SUPPLEMENTARY INFORMATION

The electron-proton bottleneck of photosynthetic oxygen evolution

Paul Greife[1#], Matthias Schönborn[1#], Matteo Capone[2#], Ricardo Assunção[1], Daniele Narzi[2], Leonardo Guidoni[2]*, Holger Dau[1]*

[1]Dept. of Physics, Freie Univ. Berlin, Germany; [2]Dept. of Physical and Chemical Sciences, Univ. of L'Aquila, Italy

[#]These three authors contributed equally.

*Corresponding authors: holger.dau@fu-berlin.de, leonardo.guidoni@univaq.it

Table of contents

SI. Supplementary Methods – Step-scan FTIR experiment 3

SI.1 Experimental set-up for step-scan FTIR with automated sample-exchange system 3

SI.2 Heat artefact correction 3

Supplementary Fig. 1 Illustrative spectra and time courses on correction for laser-induced heating 4

SI.3 Aging of the PSII samples for prolonged experimentation 5

Supplementary Fig. 2 Stability of PSII function for up to 60 hours as judged from S-state difference spectra 5

SI.4 Primary FTIR data analysis 5

SI.5 Pure S-state transitions by deconvolution 6

Supplementary Fig. 3 Spectra and time courses illustrating S-state deconvolution 9

SI.6 Correction for acceptor side contributions 11

Supplementary Fig. 4 Correction for acceptor side contributions of the DAS of the oxygen-evolution step 11

SI.7 Simulation parameters for O2-evolution transients from time-resolved polarography 13

Supplementary Fig. 5 complete sets of fit parameters in simulation of the O2-evolution transients 13

SII. Supplementary Discussion – Computational Chemistry 15

SII.1 Exploring protonation states of carboxylate groups in the S3 steady state – Glu61 (D61) 15

Supplementary Fig. 6 Geometry optimization analysis of an Asp61 protonation 15

SII.2 Exploring protonation states of carboxylate groups in the S3 steady state – Glu65 (E65) 16
Supplementary Fig. 7 Electrostatic stabilization favoring deprotonated E65 17
Supplementary Fig. 8 Comparison between X-ray structure and computationally optimized structures 17
Supplementary Tab. 1 Interaction distances of the E312 hydrogen bond network 18
SII.3 Possible role of Lys317 18
Supplementary Fig. 9 Molecules included in the QM region and shown in the video file 19
SII.4 Video of nuclear movements associated with the minimum energy path of peroxo-bond formation (information on the video provided as a separate file) 19

SIII. Supplementary Data – Tables providing further simulation parameters 20

Supplementary Tab. 2 Fit parameters for the transients shown in Figure 1 and Extended Data Fig. 2 20
Supplementary Tab. 3 Time constant values for S-state cycle reactions from previous investigations 21

References 22

SI. Supplementary Methods – Step-scan FTIR experiment

SI.1 Experimental set-up for step-scan FTIR with automated sample-exchange system

The experimental setup consists of a commercial FTIR spectrometer (Bruker, Vertex 70) modified with an extended sample chamber and temperature control device, as illustrated in the top panel of Extended Data Fig.1. The beam path of the spectrometer has been modified to include two IR filters (Quantum design) were used, a low-pass with 73% transmission at 1100 cm^{-1} and a high-pass with 80% transmission at 1800 cm^{-1}, separating the sample chamber from the interferometer and detector sections, respectively. These bandwidth limiting filters facilitates undersampling of the interferometer positions resulting in a reduced number of 334 positions for a two-sided interferogram. The two IR filters also act as visible-light filters blocking the visible-light excitation laser flash.

Two ellipsoidal focusing mirrors focus the IR beam onto a sample spot, resulting in a focused IR-beam with a diameter of 1.6 mm. The diameter of the spot illuminated by nanosecond flashes of the visible-light laser exceeded the IR-spot diameter. The visible-light laser was a pulsed frequency-doubled NdYag laser (532 nm, ca. 5 ns FWHM). In preliminary experiments, the pulse energy was adjusted for full saturation of the photosynthetic reactions. Timing of data acquisition and excitation laser was handled by a multi-channel pulse generator; for a timing diagram, see Extended Data Fig. 1. Self-written software (in C#) orchestrates the movement of the sample exchanger, refilling of the nitrogen Dewar to control the temperature, triggering of the pulse generator, and sends commands to the spectrometer through the HTML interface of the Vertex system.

SI.2 Heat artefact correction

All experimental data was processed and analyzed using Python, with standard Python toolboxes and scripts adapted for implementation of the equations and data analysis procedures described in the Methods section of the article and in the Supplementary Material, in the following sections.

Correction for heat-induced changes in spectra due to temperature changes as caused by absorption of the exciting laser-flash light is essential for proper evaluation and interpretation of time-resolved FTIR data. Supplementary Fig. 1 illustrates the effect of the phenomenon, with a significant influence within 100 µs after the laser flash. Therefore, we approached a series of experiments for determination of the artifact contribution and subsequent correction of the step-scan data set that has been collected as describe above. Briefly, a PSII sample was prepared for FTIR measurements without variation of the protocol described above, but without any artificial electron acceptor. Thirty pre-flashes were applied to each sample spot to completely reduce the native quinone electron acceptors, thereby ensuring that subsequent flashes can no longer induce light-driven charge separation by the PSII particles. At each interferogram mirror position, three excitation flashes with about 2.4 times the laser-flash energy used for data collection on functional PSII were applied at 15 Hz laser-flash frequency. In repetitions of these experiments, we observed undesired signal contributions of variable strength, possibly assignable to formation of carotenoid triplet states. We corrected for these signal contributions by difference calculations, exploiting that the undesired signals are observable with reproducible spectral

shape but variable amplitude. A resulting spectrum that represents the thermal artifact at 9 µs after application of the excitation flash is shown in Supplementary Fig. 1 a. We verified that (i) the time evolution of the thermal artifact is uniform across its spectrum and (ii) corresponds exactly to the time course of a thermal artefact signal visible with equal strength in all interferograms signals. Then the time evolution was extracted as the average of the interferograms, which is shown in Supplementary Fig. 1 b. This extracted, time-resolved thermal artifact was then fitted to the regular step-scan data set by minimizing the sum of least squares simultaneously. The spectral and temporal results are shown in Supplementary Fig. 1 a, c-f. The effects range from minimal influence in the carboxylate stretch region to a complete reversal of the trend in other regions, potentially casting doubt on the source of these early kinetics. However, a closer examination of the results shows a clear four-period behavior with different early kinetics. This is particularly clear at 1571 cm^{-1}, where the first and fifth flashes are stagnant (Supplementary Fig. 1 f) and the third and seventh flashes (Supplementary Fig. 1 e) show an increase.

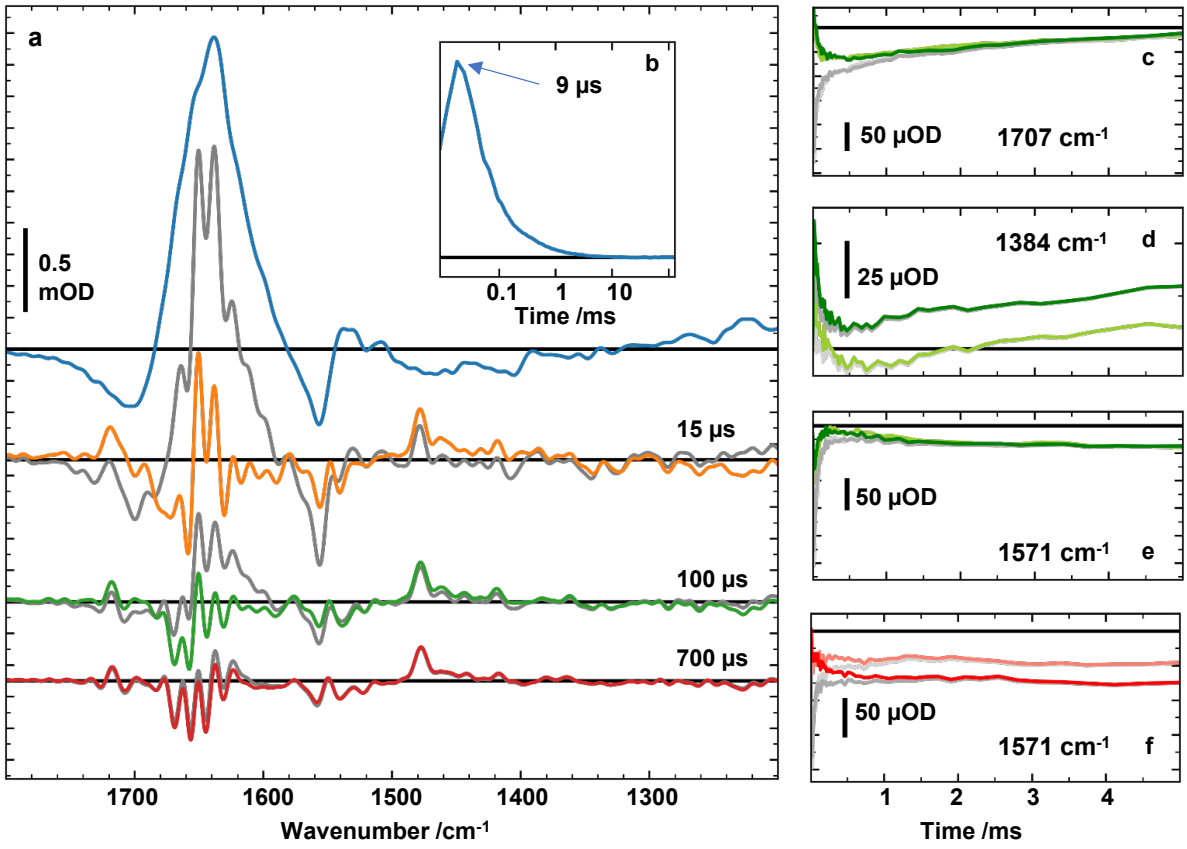

Supplementary Fig. 1. Illustrative spectra and time courses on correction for laser-induced heating (heat artifact, see above text). In **a**, blue, scaled heat artefact spectrum; grey, uncorrected third flash spectra at various times; colored, heat artefact corrected third flash spectra. In **b**, heat artefact transient recorded at center-burst position of the interferogram, note the logarithmic time axis. In **c-f**, third-flash (dark green) and seventh-flash (light green) corrected transients and (grey lines) uncorrected transients.

SI.3 Aging of the PSII samples for prolonged experimentation

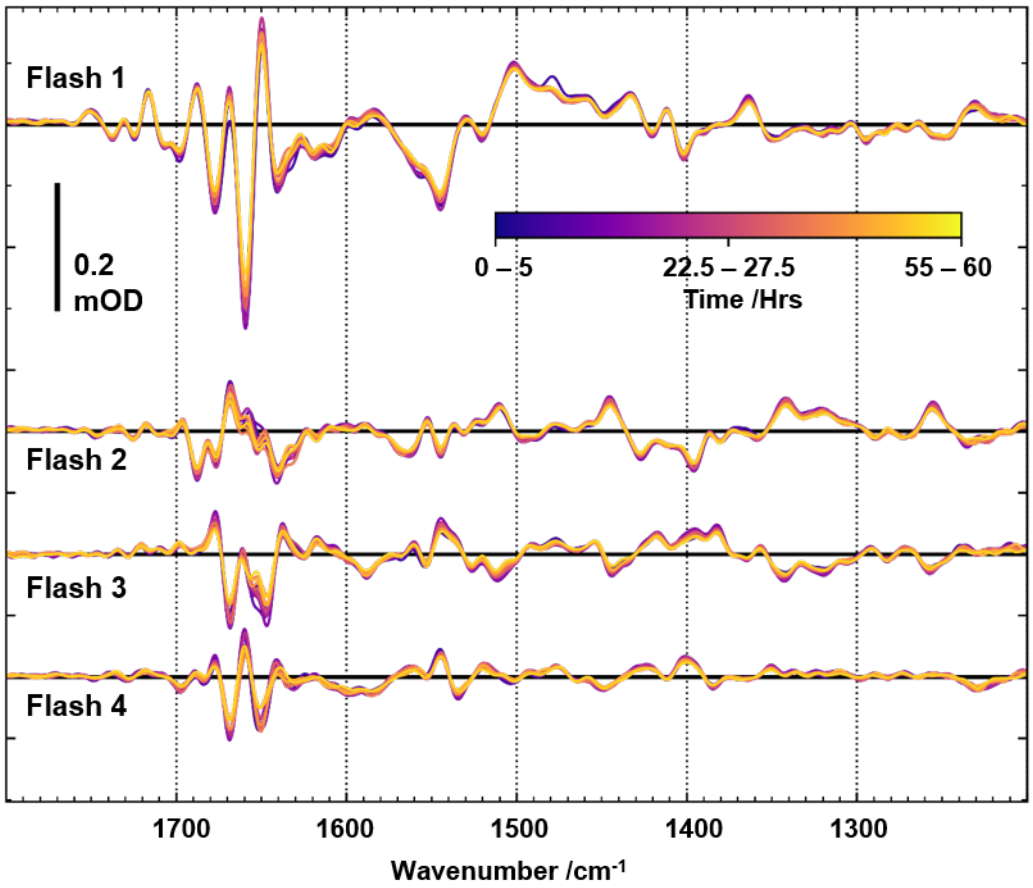

Supplementary Fig. 2. Stability of PSII function for up to 60 hours as judged from S-state difference spectra. A rapid-scan measurement recorded with a spectral resolution of 10 cm^{-1} (at 10°C) over several days, averaged in batches of 5 hours. Each batch contains roughly 1000 flash sequences of 10 excitation flashes applied with a flash spacing of 700 ms. The remaining measurement parameters are identical to those described in the Materials and Methods section. The shown data demonstrates that spectral differences between the different batches collected over a time period of 60 hours are negligible.

SI.4 Primary FTIR data analysis

Step-scan transients were normalized to rapid-scan interferogram counterparts, to account for variations in sample thickness. Prior to averaging, a Forman phase correction was applied to stitched interferograms.[1] The phase correction uses a truncated interferogram to calculate the phase spectrum and correct for mismatches in the interferogram between data sets. Here, of the original 334 mirror positions only the central 320 are used to calculate the phase spectrum. To calculate the location of the center burst, the positions of the minimum and maximum values were averaged and rounded. We observed oscillatory noise contributions of the IR transients resulting from small oscillations in the center-burst position of the interferometer caused by acoustically excited small-amplitude oscillation of the interferometer mirror position. These were effectively minimized by setting the absorption change for the six mirror positions closest to the center burst to zero. We verified by simulation that,

as expected, there was no effect on the time-resolved spectra itself aside from the (desirable) removal of broad background features.

To reduce data set size, the transients (time courses) at the respective wavenumber were averaged such that the number of data points per decade was 24, with equidistant position of the data point on a logarithmic time axis (logarithmic averaging; for 69 µs before and 153 µs after the laser flash, the logarithmic averaging was not applied). The real component of the Fast Fourier Transform (FFT) was computed and the infrared absorption calculated.

SI.5 Pure S-state transitions by deconvolution

By application of 10 light flashes in our FTIR experiment, the PSII cycle up to 2.5 times through the four semi-stable intermediates of the S-state reaction cycle. The cycling does not proceed fully synchronized because of 'miss events' that result in less-than-unity efficiency (Φ) of advancement in the S-state cycle (Φ = 100% - *m*, where *m* is the 'miss factor'). We developed a deconvolution procedure that takes into account all the IR transients collected starting from the 2nd flash up to the 10th flash. By omitting the first flash from the analysis, we ensured that events taking place exclusively on the first flash do not affect the results of our analysis, specifically the stable (for several seconds) formation of reduced primary quinone acceptor (Q_A^-) in photosystems without a functional Q_B site.

Let $P_{i,j}$ be the matrix representing the population, where *i = 0,1,2,…I* is the flash number and *j = 1,2,3,0* represents the S-states. Before the first flash, it is assumed that the initial population is shared between the S_1 and S_0 states $P_0 = (1\text{-}P_{S0},0,0,P_{S0})$. Subsequent flash populations can be calculated using the propagation matrix *M*(*m*) with miss factor *m.*

$$P_{i+1}(m) = M(m) \cdot P_i = \begin{pmatrix} m & 0 & 0 & 1-m \\ 1-m & m & 0 & 0 \\ 0 & 1-m & m & 0 \\ 0 & 0 & 1-m & m \end{pmatrix} \cdot P_i = (M)^{i+1} \cdot P_0$$

The above population vector contains the distribution of the photosystems across each of the four S-states after the ith flash. The signal registered at the detector, *R*, differs from the population propagation because only those photosystems that successfully transition are assumed to contribute. This means that a modified version of the matrix *M*, representing only those centers participating in a transition, must be applied to the vector P_i to calculate the contribution of each S-state to the signal induced by the i+1 flash.

$$R_{i+1}(m) = \begin{pmatrix} 0 & 0 & 0 & 1-m \\ 1-m & 0 & 0 & 0 \\ 0 & 1-m & 0 & 0 \\ 0 & 0 & 1-m & 0 \end{pmatrix} \cdot P_i$$

Note that this participation matrix is simply the propagation matrix M(m) with zeros along the diagonal, as it is assumed that centers experiencing a 'miss' do not contribute to the signal.

The flash dependent amplitudes $A_{i,\nu}$, where ν is the wavenumber, can be derived from the S-state eigenvalues α_j and the signal matrix $R_{i,j}$.

$$A_{i,\nu} = R_{i,j} \cdot \alpha_\nu^j$$

To solve for α, a matrix inversion must be applied to a symmetric matrix

$$R^T \cdot A = R^T \cdot R \cdot \alpha$$

$$\alpha = (R^T \cdot R)^{-1} \cdot R^T \cdot A$$

The element ($R^T \cdot R$) is degenerate so the pseudo-inverse must be approximated using a least-squares solver. The miss factor m found by calculating the difference between A_ν and the simulated $A_\nu(m)$ and minimizing the sum of their squares:

$$\left(\sum_{i,\nu} A_{i,\nu} - A'_{i,\nu}(m)\right)^2 = \left(\sum_{i,\nu} A_{i,\nu} - R \cdot (R^T \cdot R)^{-1} \cdot R^T \cdot A_{i,\nu}\right)^2 \to 0$$

In addition, extended dark-adaptation periods cannot ensure that all PSII are in the dark-stable S_1 state. Minor contributions of further S-states (specifically the S_0 state) were considered, as described in the following. The long-time dark-stable S-States are S_1 and S_0; as such it was assumed that the initial population in other states was negligible. In the S_1 -> S_2, S_2 -> S_3 and S_0 -> S_1 transition, the millisecond phase corresponds to the redox reaction between Q_A and PPBQ. As the two electron quinone chemistry repeats itself after a two S-state transitions it was assumed that the corresponding decay associated spectra, $\alpha_\tau^{i->i+1}$ of the S_2->S_3 transitions should look very similar to its parallel in the S_0->S_1 transition.

$$\alpha_{1.7ms}^{S2\to S3} \approx \alpha_{1.7ms}^{S0\to S1}$$

During the S_3 -> S_0 transition, this phase happens to be concurrent with the dominating oxygen-evolution phase. As such, it will be the most different of the four transitions, with unique O-O bond formation features alongside the quinone features. These similarities and differences can be observed in Supplementary Fig. 3f.

$$\alpha_{2.7ms}^{S3\to S0} = \alpha_Q^{S3\to S0} + \alpha_{O2}^{S3\to S0}$$

The components of the S_3->S_0 DAS corresponding to quinone chemistry should be also very similar to that of the S_1->S_2 transition.

$$\alpha_{Q}^{S3\rightarrow S0} \approx \alpha_{1.7ms}^{S1\rightarrow S2}$$

Exploiting this pattern and the unique signals seen in the S_3->S_0 transition the fraction of centers starting in the S0 state, PS0 was approximated by minimizing the ratio of the difference between the millisecond DAS the S_2 -> S_3 and S_0 -> S_1 transitions while maximizing the difference between the S_1 -> S_2 and S_3 -> S_0 transitions.

$$\min\left(\frac{\sum_{\nu}\left|\alpha_{1.7ms}^{S2\rightarrow S3}-\alpha_{1.7ms}^{S0\rightarrow S1}\right|}{\sum_{\nu}\left|\alpha_{2.7ms}^{S3\rightarrow S0}-\alpha_{1.7ms}^{S1\rightarrow S2}\right|}\right)$$

Thereby the parameters for S-state deconvolution were obtained. The deconvolution resulted in corrected transients, which correspond to 'pure' S-state transitions. For deconvolution, flashes 2 through 10 were used with a miss factor of 13.8% and initial S-state population of 87.7% S_1/12.3% S_0.

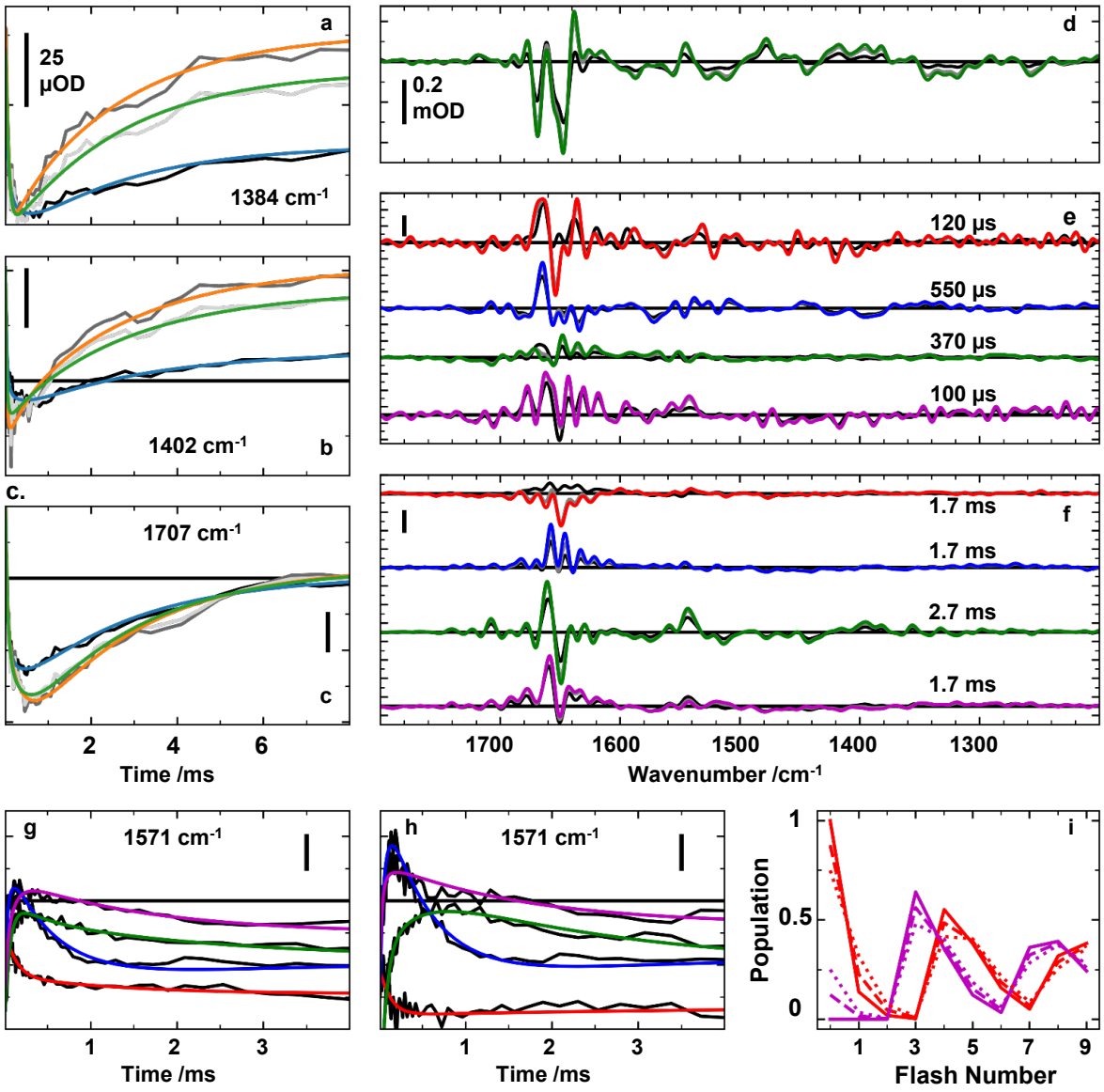

Supplementary Fig. 3. Spectra and time courses illustrating S-state deconvolution, that is, the correction for impure S-state populations as they result from imperfectly synchronized advancement in the S-state cycle.

a, b, c. Transients comparing the effect of the deconvolution on the S_3 -> S_0 (3rd flash) transition with different starting populations at various wavenumbers. Blue, 'raw' (as measured) 3rd flash transient; green, S_3 -> S_0 deconvoluted transient with 100% S_1 starting population; orange, S_3 -> S_0 deconvoluted transient with 87.7% S_1 and 12.3% S_0 starting populations.

d. S_3 -> S_0 Spectra at 130 ms after the flash. Black, 'raw' 3rd flash spectrum; grey, S_3 -> S_0 deconvoluted spectrum with 100% S_1 starting population; green, S_3 -> S_0 deconvoluted spectrum with 87.7% S_1 and 12.3% S_0 starting populations.

e. Decay-associated spectra corresponding to the ~100 µs time constants of each transition. Colored, DAS spectra with 87.7% S_1 and 12.3% S_0 starting population; grey, 100% S_1 deconvolution variants; black, 'raw' flash data fitted with the same time constants as found in the deconvoluted counterparts. In descending order, S_1 -> S_2 (red), S_2 -> S_3 (blue), S_3 -> S_0 (green), S_0 -> S_1 (magenta). Note the good agreement of the S_1 -> S_2 and the 1st flash spectra.

f. Decay-associated spectra corresponding to the 1-3 ms processes in each transition (color code as in **e**). Note the poor agreement of the S_1 -> S_2 and the 1st flash spectrum, which relates to specifics

of the acceptor side processes visible on the 1st flash only. Therefore, exclusively flashes 2 through 10 were used for obtaining pure S-state spectra by deconvolution.

g. 'Raw' transients at 1571 cm^{-1}. In red, 1st flash; blue, 2nd flash; green, 3rd flash, magenta, 4th flash.

h. 87.7% S_1 and 12.3% S_0 deconvoluted transients at 1571 cm^{-1}. In red, S_1 -> S_2 ; blue, S_2 -> S_3; green, S_3 -> S_0; magenta, S_0 -> S_1.

i. simulation of the S_1 (red) and S_0 (magenta) state populations following each flash with different starting parameters. Solid line, 100% S_1 and 0% S_0, dashed line, 87.7% S_1 and 12.3% S_0, dotted line, 75% S_1 and 25% S_0.

SI.6 Correction for acceptor side contributions

Concomitant to the oxygen evolution step of the S_3 -> S_0 transition, there are acceptor side processes associated with quinone reactions. While relatively small, the acceptor side contributions complicate interpretation of the spectra. Unlike the period-of-four pattern in the flash-number dependence of the S-state cycle reactions, the acceptor side functions with a period of two. Features of the 3.1 ms phase of the S_1 -> S_2 transition should then represent the same changes as the process in the S_3 -> S_0 transition. Analogous to the simulations of the S_3 -> S_0 transition, the S_1 -> S_2 transition was simulated using a multi-exponential function. The decay associated spectra of the 3.1 ms phase was then subtracted, without scaling, from 2.5 ms DAS of the S_3 -> S_0 transition. The effect of this operation becomes clear in two key regions: (1) between 1460 cm^{-1} and 1500 cm^{-1} two features associated with the quinone redox reactions become significantly smaller; (2) bands above 1700 dipping below the zero-line are shifted up, clarifying their position and significance to the oxygen evolution step. To test the validity of this approach a time resolved spectrum of the 3.1 ms phase of the S_1 -> S_2 transition was simulated and subtracted from the time resolved S_3 -> S_0 data. Simulation parameters are summarized in Supplementary Tab. 2.

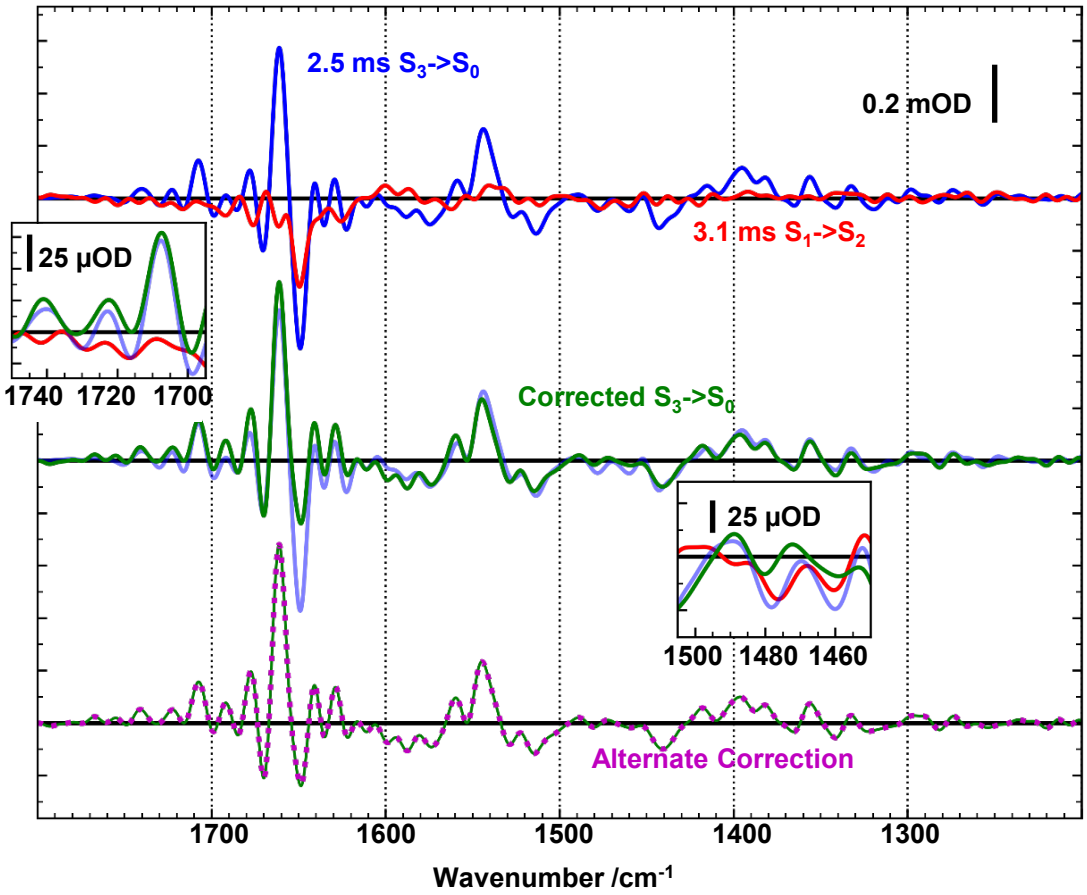

Supplementary Fig. 4. Correction for acceptor side contributions of the DAS of the oxygen-evolution step. Top: Comparison of the 2.5 ms / S_3 -> S_0 DAS (blue) and the 3.1 ms / S_1 -> S_2 DAS (red). Middle: Comparison of acceptor side corrected S_3 -> S_0 DAS (green) with the uncorrected DAS (blue). The correction is a simple subtraction of the S_1 -> S_2 DAS from the S_3 -> S_0 DAS. Of note is the region above 1700 cm^{-1} where spectral peaks move to the zero line and around 1470 cm^{-1} when features associated with the acceptor side disappear (see inserts). Bottom: Comparison of two correction methods. In green, the result of subtracting the acceptor side 3.1 ms / S_1 -> S_2 DAS from the 2.5 ms / S_3 -> S_0 DAS

associated with the rate-determining step in O_2-formation. In red, an alternative where the 3.1 ms / S_1 -> S_2 DAS is used to simulate a transient and is then subtracted from the time-resolved S_3 -> S_0 data. Following this operation, the data is simulated with a time constant at 2.5 ms, representing the rate-determining step in O_2-formation. The two correction modes lead to a highly similar result.

SI.7 Simulation parameters for O_2-evolution transients from time-resolved polarography

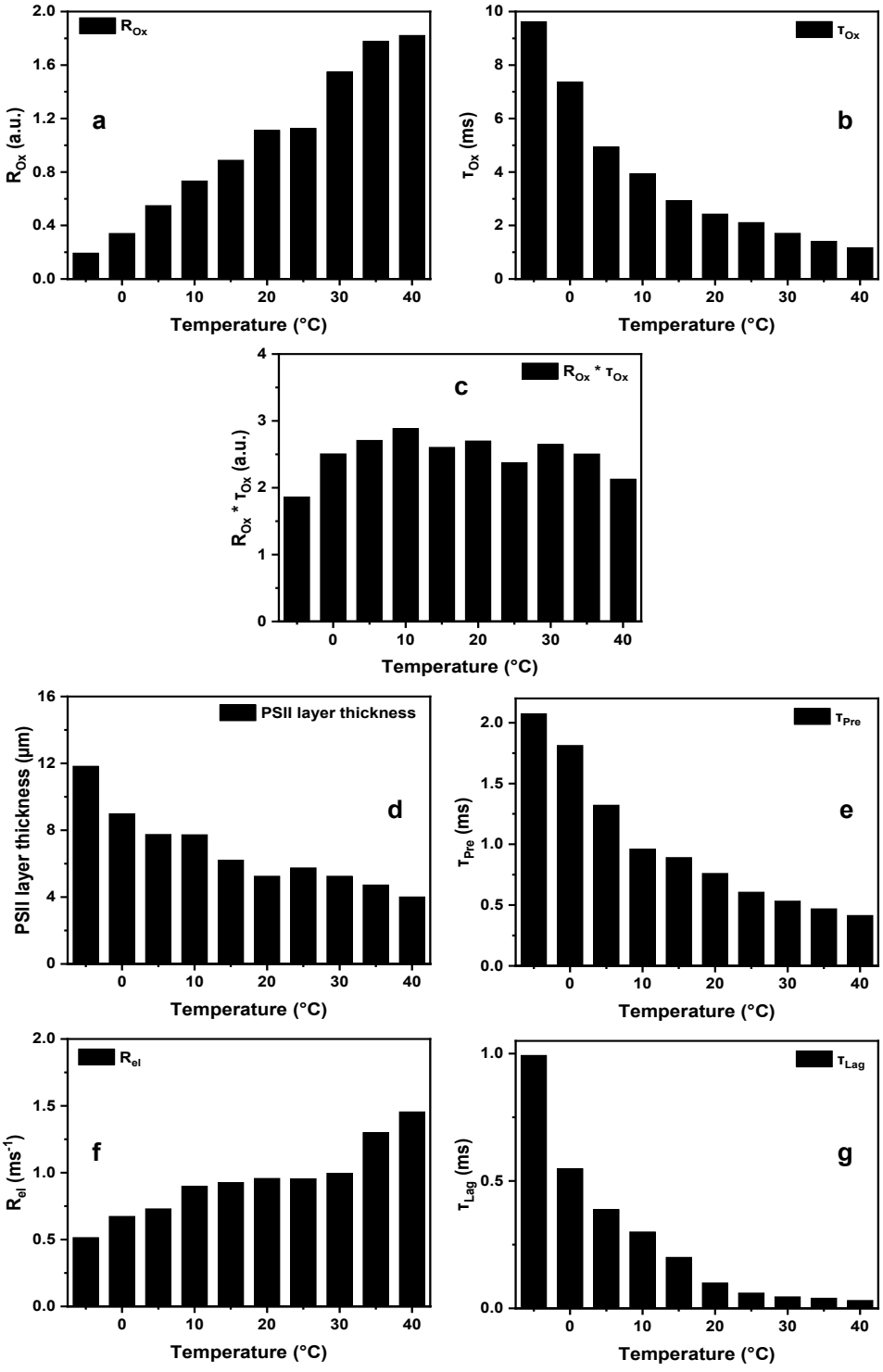

Supplementary Fig. 5. The complete sets of fit parameters in simulation of the O_2-evolution transients of Extended Data Fig. 5. **a**. Parameter that scales with the rate of O_2-formation (R_{ox}). **b.** Time constant (inverse rate constant) of oxygen evolution by PSII (τ_{O2}). **c**. Product of R_{ox} and τ_{O2}, a quantity that is proportional to the flash yield of O_2-formation (proportional to the total amount of O_2 molecules that are formed). The O_2 flash yield has been found to be slightly temperature dependent only, with maximal flash yield (minimal miss parameter) around 10°C [2], in the line with the behavior visible in

panel c. This agreement between fit parameters and expected behavior strengthens the confidence in the simulation results. **d.** Apparent thickness of the layer of PSII membrane particles deposited by centrifugation on the bare platinum electrode, assuming tabulated values for the O_2-diffusion constant of pure water. The seeming temperature dependence of the layer thickness reflects the temperature dependence of the O_2 diffusion constant of the layered PSII membrane particles. **e** and **g** show the parameters τ_{pre} and τ_{lag}, which describe the delayed onset of the O_2-evolution transients. To both, τ_{pre} and τ_{lag}, the delayed onset of O_2-formation by PSII as well as the electrode response contribute. **f**. The R_{el} parameter corresponds to the rate constant of O_2 reduction at the bare platinum electrode, which increases with increasing temperature.

SII. Supplementary Discussion – Computational Chemistry

SII.1 Exploring protonation states of carboxylate groups in the S_3 steady state – Glu61 (D61)

The protonation state of Asp61 in the S3 steady state has been investigated by means of ab-initio geometry optimization of the crystallographic structure resolved by Kern et al. [Kern2018], starting with a protonated Asp61 carboxylate and W1 in its hydroxide form, as shown in Supplementary Fig. 6.

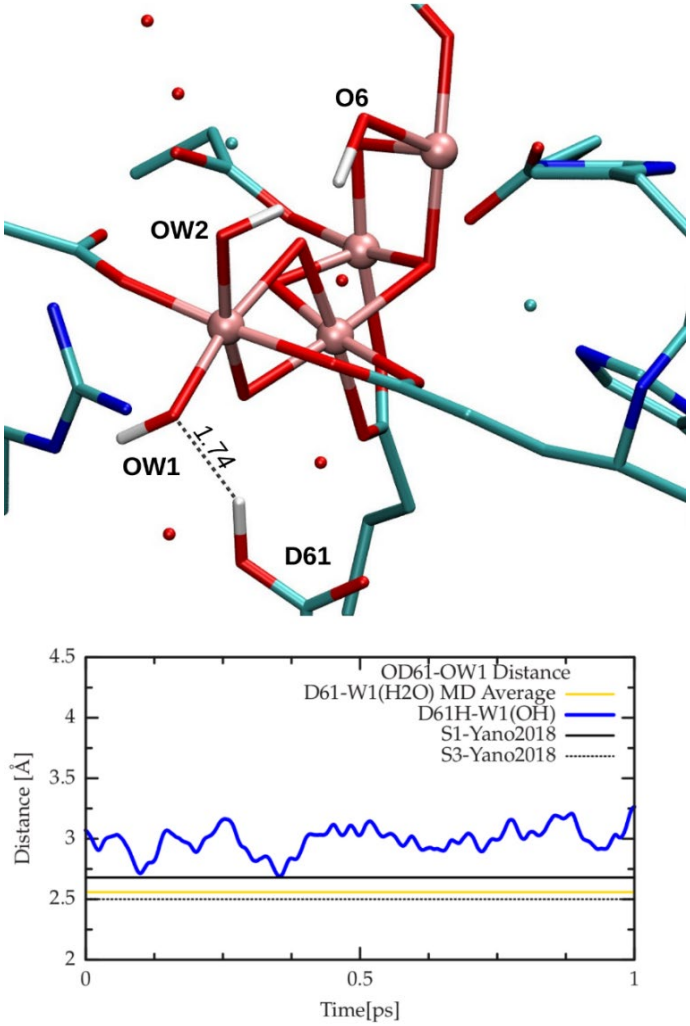

Supplementary Fig. 6. Top panel: Starting positions of the geometry optimization to analyze the reliability of an Asp(D)61 protonation. After few iterations of the geometry optimization the bond between the proton and the carboxylic oxygen of Asp61 is broken, and the water form of W1 molecule restored. Bottom panel: Distance between the hydrogen bonding oxygens of Asp61 and OW1 in a QM/MM MD simulation after 1 ps of distance restraint. The higher value of such distance with respect to x-ray is stable in the picosecond of the free simulation, corresponding to a different hydrogen bonding network. The distance values are compared with the crystallographic distances in S_1 and S_3 from ref.[3] and with the average distance calculated along 10 ps of a QM/MM MD simulation with deprotonate Asp61.[4]

Notably, in the first steps of geometry optimization the proton jumps back to the W1 molecule leaving Asp61 in its deprotonated form, thus indicating the instability of such protonation pattern relatively to the experimental structure of the S_3 steady state. The assumption made in previous theoretical studies

indicating a deprotonated state for Asp61 in different steady states of the Kok cycle, is therefore supported also by the local stability of the hydrogen bond network explored by our ab initio calculations based on the crystallographic positions of the S_3 state. Additionally, to overcome local energy barriers and check other possible energy minima corresponding to a protonated form of Asp61, we also performed 1 ps of QM/MM MD simulation, restraining the proton to be bound to Asp61. After 1 ps of restrained QM/MM MD simulation, the restrain was removed and the system left free to evolve for one additional ps. In this time the proton remained bound to Asp61 leaving the W1 water molecule in its hydroxide form. Nevertheless, the distance between the carboxylate oxygen of Asp61 and the OW1 oxygen, was found to diverge significantly from that found in the x-ray structure. On the other side, a previous QM/MM MD simulation of the S_3 state, carried out for 10 ps, considering Asp61 deprotonated [4], showed an average value much closer to the crystallographic value, when compared with the values of the simulation employed with protonated Asp61 (see bottom panel Supplementary Fig. 6).

SII.2 Exploring protonation states of carboxylate groups in the S_3 steady state – Glu65 (E65)

Protein crystallography suggest a short distance between carboxylate oxygen atoms of Glu65 and Glu312 in H-bonding distance of well below 3 Å. Consequently, the H-bonding proton is associated preferentially either with Glu65 or with Glu312. In ref.[5], Ishikita and corkers assume that Glu65 is preferentially protonated, in line with their calculations. We consider this option as unlikely, due to the evident stabilization of the deprotonated form of Glu65 arising from the interaction with Arg334 and Asn335. See Supplementary Fig. 7, where we report the distances between such moieties as found in the S_3 crystal structure (see also Supplementary Tab. 1). In line with this observation, empirical pKa calculations carried out with Propka software [ProPka] on the S_3 structure resolved by Kern et al., also confirm a preferential deprotonated state for Glu65, while suggest a protonated form for Glu312 (i.e. pK_a = 7.2 for Glu312 and 2.4 for Glu65).

To provide further support for Glu312 protonation, we performed QM geometry optimizations on a larger system including atoms of Lys317, Glu312, Glu65, Arg334, Asn335 and their closest water molecules, as found in the X-ray structure [Kern2018]. In Fig. SII.3 the structural effects arising from the protonation/deprotonation of Glu312 are reported and compared with the crystallographic positions.

In our model the absence of a proton in the carboxylate group of Glu312, has a clear impact on the position of the Glu65 side chain, making it to diverge from its crystallographic position, due to the electrostatic repulsion between the two negative glutamate residues (left panel Supplementary Fig. 8). Conversely, the protonation of Glu312 strongly preserves the X-ray positions after Full-QM geometry optimization (right panel Supplementary Fig. 8). In Tab. S1 are reported the RMSD of the atomic coordinates of the two models with respect to the crystallographic positions. The largest value is observed for the case of the model with deprotonated Glu312.

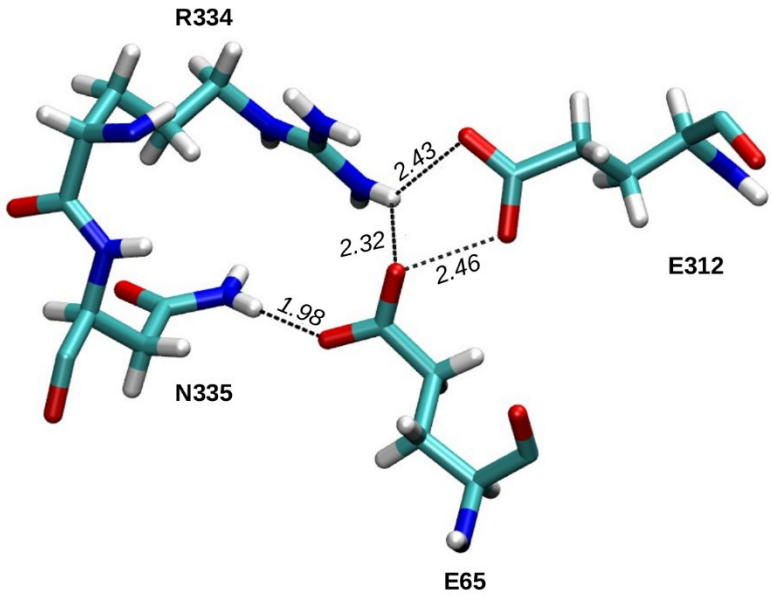

Supplementary Fig. 7. Electrostatic stabilization favoring deprotonated Glu65. ´The Glu(E)312 – Glu(E)65 – Arg(R)334 – Asn(N)335 sidechain distances as found in the crystallographic data from Kern et al.[3] are indicated.

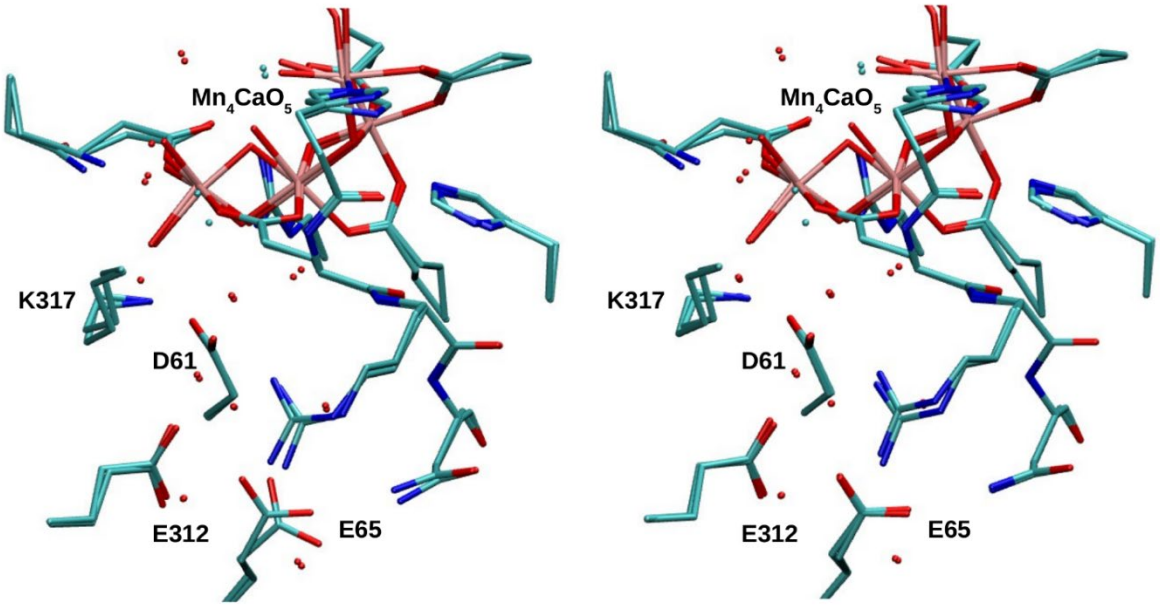

Supplementary Fig. 8. Comparison between X-ray structure [Kern2018] and computationally optimized structures. For the sake of clarity, the hydrogen atoms are hidden. The two shown models differ only by the protonation of Glu(E)312. On the left, the computational Glu312-deprotonated model is compared with the X-ray structure (RMSD of 0.315 Å), whereas on the right the Glu312-protonated model is compared with the same X-ray structure (RMSD of 0.271 Å).

Supplementary Tab. 1. Interaction distances of the Glu312 hydrogen bond network.

Distance / State	S_1	S_2	S_3
Glu65-Glu312 (O-O)	2.42	2.55	2.46
Arg334-Glu65 (NH-O)	2.87	2.68	2.32
Arg334-Glu312 (NH-O)	2.35	3.01	2.43
Asn335-Glu65 (NH-O)	2.08	2.04	1.98
Lys317-Asp61 (NH-O)	3.97	3.90	4.16

SII.3 Possible role of Lys317

The possibility of a mechanistically relevant electrostatic interaction between Lys317 and Asp61 is apparent, due to their short distance (see Extended Data Fig. 9A). Electrostatic stabilization of $Lys317^+$ on $Asp61^-$ could prevent an easy and fast protonation of the aspartic residue, therefore preventing its protonation in the S_3 steady state. We assume that deprotonation of Glu312, upon Tyr_Z radicalization, could be coupled to reorientation of the positive Lys317 side chain towards the negative Glu312 side chain. In this way, the deprotonation of Glu312, could promote the subsequent Asp61 protonation, distancing the positive Lys317 side chain from it and therefore increasing its pKa. Alternatively, Tyr_Z radicalization with the formation of the positively charged Tyr-Z/$His190^+$ moiety, could directly induce a reorientation of the Lys317 side chain towards Glu312, thus simultaneously increasing the pK_a of Asp61 and promoting the deprotonation of Glu312.

To support our hypothesis we show that the side chain of Lys317 indeed can structurally sample conformations strongly interacting either with Asp61 or with Glu312. In this regard we monitored the distances between Lys317 and both Asp61 and Glu312, along 50 ns of two classical MD simulations (Extended Data Fig. 9B,C,D,E). The two simulations differ only for the protonation state of Glu312, deprotonated in Simulation 1 and protonated in Simulation 2. In both simulation Asp61 is deprotonated. Our analysis shows that the side chain of Lys317 preferentially remains close to Glu312 in Simulation 1 (deprotonated Glu312), while preferentially interacts with Asp61 in Simulation 2. Albeit not quantitatively reliable, these results qualitatively show, from a structural point of view, the possibility of Lys312 to potentially interact either with Asp61 or with Glu312, depending on the protonation state of Glu312. Therefore, these findings lead support to a possible role of Lys312 in modulating the protonation/deprotonation of the neighbor residues Asp61 and Glu312 and ultimately the release of the proton from the catalytic center.

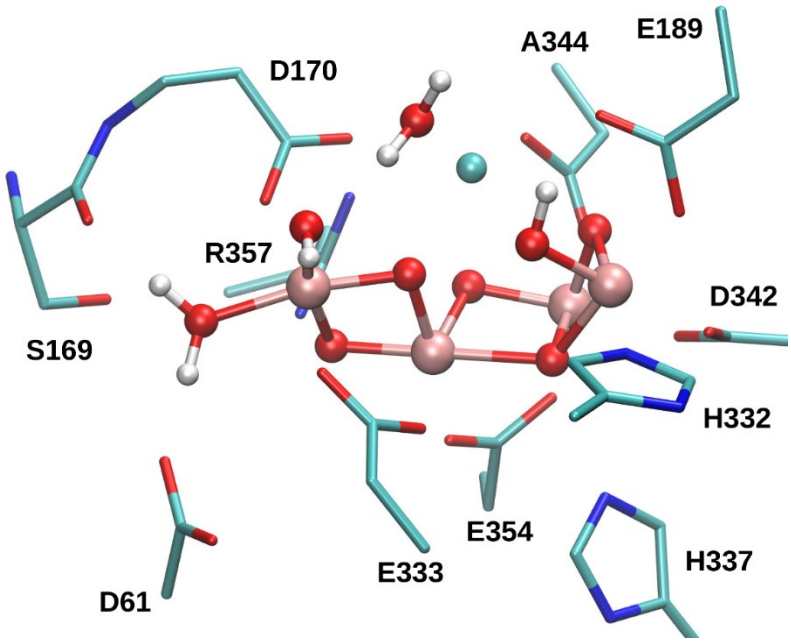

Supplementary Fig. 9. Mn_4Ca-oxo cluster, water molecules and protein residues included in the QM region and shown in the video file (the labels are not shown in the video). All the water molecules and the hydrogen atoms that are not directly involved in the considered reaction pathway have been removed for clarity.

SII.4 Video of nuclear movements associated with the minimum energy path of peroxo-bond formation.

As supplementary data, a video is included (separate mp4 file) that shows the atomic displacement associated with the minimum energy path (MEP) calculations discussed in the main text. The included amino acid residues are shown with labels in Supplementary Fig. 9.

SIII. Supplementary Data – Tables providing further simulation parameters

Supplementary Tab. 2. Fit parameters for the transients shown in Fig. 1 and Extended Data Fig. 2, for all four S-state transitions. Time constants marked with a * were set constant while all others were allowed to vary. Due to the fit ansatz described in the materials and methods the offset represents the starting value of the transients immediately after the flash (t = 0 s). Amplitudes and offset values are provided in µOD.

S_1 -> S_2	Offset	33 µs		91 µs	3.1 ms	25 ms
1384 cm^{-1}	110	-31		-72	10	11
1402 cm^{-1}	76	1.0		-180	-1.7	19
1449 cm^{-1}	8.4	-15		58	6.5	-28
1568 cm^{-1}	33	-57		-110	-15	58
1706 cm^{-1}	-17	-73		55	-17	36
S_2 -> S_3		43 µs		290 µs	1.8 ms	23 ms*
1384 cm^{-1}	-14	52		-59	14	2.3
1402 cm^{-1}	77	-22		-56	44	22
1449 cm^{-1}	93	-98		77	14	-5
1568 cm^{-1}	-110	172		-100	34	22
1706 cm^{-1}	55	-140		11	66	8.5
S_3 -> S_0		26 µs	65 µs	340 µs	2.5 ms	22 ms
1384 cm^{-1}	105	-3.3	-98	0.3	73	-4.9
1402 cm^{-1}	93	-120	3.4	59	71	6.4
1449 cm^{-1}	61	-5.7	-12	-24	-27	-12
1568 cm^{-1}	-130	57	-26	80	-58	64
1706 cm^{-1}	51	-41	-27	-100	127	-3.5
S_0 -> S_1		28 µs		150 µs	1.5 ms	23 ms*
1384 cm^{-1}	21	-60		-31	26	6.6
1402 cm^{-1}	34	-6.5		-13	16	7.0
1449 cm^{-1}	90	-70		-29	19	7.5
1568 cm^{-1}	-48	58		20	-48	8.4
1706 cm^{-1}	79	-52		-100	51	24

Supplementary Tab. 3. Time constant values for S-state cycle reactions from previous investigations. The first τ-column provides the time constant values determined in the respective study at the measurement temperature indicated in the second column. The corresponding value at 10 °C were calculated from the first-column values using the respective activation energy as reported in ref.[6]; they are provided in the third column (τ_{10}). Exclusively time constant values are listed which we previously determined using the same protocols for preparation of high-activity PSII membrane particles as used in the present investigation. Comparison of curve-fit results from the various studies suggests a sizeable uncertainty range. Within the limits of the uncertainty present also in the previously reported values, the time constant values of the present investigation agree satisfactorily well with previously reported results.

	τ	Temperature \°C	τ_{10} (at 10°C)	Method	Reference
S_1 -> S_2	120 µs	10	120 µs	photothermal	ref. [6]
	100 µs	23	133 µs	UV-visible	ref.[7]
S_2 -> S_3	60 µs	10	60 µs	photothermal	ref. [6]
	25 µs	RT (25)	66 µs	X-ray absorption	ref.[8]
	320 µs		673 µs	X-ray absorption	
	18 µs	10	18 µs	delayed fluorescence	ref.[9]
	100 µs		100 µs	delayed fluorescence	
	330 µs		30 µs	delayed fluorescence	
	280 µs	23	535 µs	UV-visible	ref.[7]
S_3 -> S_0	200 µs	RT (25)	290 µs	X-ray absorption	ref.[10]
	14 µs	20	18 µs	delayed fluorescence	ref.[11]
	65 µs		84 µs	delayed fluorescence	
	200 µs		257 µs	delayed fluorescence	
	170 µs	23	235 µs	UV-visible	ref.[7]
	1.7 ms		2.6 ms	UV-visible	
	25 µs	20	32 µs	photothermal	ref.[12]
	250 µs		322 µs	photothermal	
	150 µs	RT (25)	217 µs	X-ray absorption	ref.[8]
	1.6 ms		2.6 ms	X-ray absorption	
	20 µs	10	20 µs	delayed fluorescence	ref.[9]
	100 µ		100 µs	delayed fluorescence	
	400 µs		400 µs	delayed fluorescence	
	2.4 ms		2.4 ms	delayed fluorescence	
	2.8 ms	10	2.8 ms	photothermal	ref.[6]
	2.2 ms	10	2.2 ms	delayed fluorescence	ref.[11]
S_0 -> S_1	50 µs	RT (25)	55 µs	X-ray absorption	ref.[8]
	160 µs	10	160 µs	photothermal	ref.[6]

References

1 Forman, M. L., Steel, W. H. & Vanasse, G. A. Correction of Asymmetric Interferograms Obtained in Fourier Spectroscopy. *J Opt Soc Am* **56**, 59-&, doi:Doi 10.1364/Josa.56.000059 (1966).

2 Grabolle, M. & Dau, H. Efficiency and role of loss processes in light-driven water oxidation by PSII. *Physiologia Plantarum* **131**, 50-63 (2007).

3 Kern, J. *et al.* Structures of the intermediates of Kok's photosynthetic water oxidation clock. *Nature* **563**, 421-425, doi:10.1038/s41586-018-0681-2 (2018).

4 Narzi, D., Capone, M., Bovi, D. & Guidoni, L. Evolution from S_3 to S_4 state of the oxygen evolving complex in Photosystem II monitored by QM/MM dynamics. *Chemistry--A European Journal* (2018).

5 Kuroda, H. *et al.* Proton transfer pathway from the oxygen-evolving complex in photosystem II substantiated by extensive mutagenesis. *Biochim Biophys Acta Bioenerg* **1862**, 148329, doi:10.1016/j.bbabio.2020.148329 (2021).

6 Klauss, A., Haumann, M. & Dau, H. Alternating electron and proton transfer steps in photosynthetic water oxidation. *Proceedings of the National Academy of Sciences of the United States of America* **109**, 16035-16040, doi:10.1073/pnas.1206266109 (2012).

7 Gerencser, L. & Dau, H. Water oxidation by Photosystem II: H_2O−D_2O Exchange and the influence of pH support formation of an intermediate by removal of a proton before dioxygen creation. *Biochemistry-Us* **49**, 10098-10106, doi:10.1021/bi101198n (2010).

8 Zaharieva, I., Dau, H. & Haumann, M. Sequential and coupled proton and electron transfer events in the S_2 -> S_3 transition of photosynthetic water oxidation revealed by time-resolved X-ray absorption spectroscopy. *Biochemistry-Us* **55**, 6996-7004, doi:10.1021/acs.biochem.6b01078 (2016).

9 Zaharieva, I., Grabolle, M., Chernev, P. & Dau, H. in *Photosynthesis Research for Food, Fuel and Future* (eds T. Kuang, C. Lu, & L. Zhang) 234-238 (Springer, 2013).

10 Haumann, M. *et al.* Photosynthetic O_2 formation tracked by time-resolved x-ray experiments. *Science* **310**, 1019-1021, doi:10.1126/science.1117551 (2005).

11 Buchta, J., Grabolle, M. & Dau, H. Photosynthetic dioxygen formation studied by time-resolved delayed fluorescence measurements--method, rationale, and results on the activation energy of dioxygen formation. *Biochimica et Biophysica Acta* **1767**, 565-574, doi:10.1016/j.bbabio.2007.04.003 (2007).

12 Klauss, A., Haumann, M. & Dau, H. Seven steps of alternating electron and proton transfer in photosystem II water oxidation traced by time-resolved photothermal beam deflection at improved sensitivity. *J Phys Chem B* **119**, 2677-2689, doi:10.1021/jp509069p (2015).